Northumbria Research Link

Standalone DC Microgrids as Complementarity Dynamical Systems: Modeling and Applications

Arash M. Dizqah[a,*], Alireza Maheri[a], Krishna Busawon[a], Peter Fritzson[b]

[a]*Faculty of Engineering and Environment, Northumbria University, NE1 8ST, Newcastle upon Tyne, UK*
[b]*PELAB - Programming Env. Lab, Linköping University, SE-581 83, Linköping, Sweden*

Abstract

It is well-known that, due to bimodal operation as well as existent discontinuous differential states of batteries, standalone microgrids belong to the class of hybrid dynamical systems of non-Filippov type. In this work, however, standalone microgrids are presented as complementarity systems (CSs) of the Filippov type which is then used to develop a multivariable nonlinear model predictive control (NMPC)-based load tracking strategy as well as Modelica models for long-term simulation purposes. The developed load tracker strategy is a multi-source maximum power point tracker (MPPT) that also regulate the DC bus voltage at its nominal value with the maximum of $\pm 2.0\%$ error despite substantial demand and supply variations.

Keywords: Nonlinear model predictive control (NMPC), Mixed complementarity problem (MCP), Wind energy, Photovoltaic (PV), Lead-acid battery, Modelica, Modeling, Maximum power point tracking (MPPT).

1. Introduction

Microgrids are the building blocks of the modern power grids. In fact, the near future distribution grids can be seen as a network of several interconnected microgrids which locally generate, consume, and even store energy [1]. Intermittent solar and wind energies, coupled with battery storages, contributes to the energy resources for supplying variable load demands of the microgrids [2]. Due to some challenges that ac microgrids face with hosting several distributed energy systems [3, 4], such as the need for synchronization, dc microgrids have gained more popularity particularly for standalone applications in avionic, automotive, or marine industries as well as the remote rural areas [1, 5]. There are various interests in employing nonlinear model predictive control (NMPC) technique [6, 7] to develop coordinated multivariable control strategies for the standalone microgrids (e.g. [8, 9]). However, such control strategies require the use of an adequate mathematical model of the microgrids in order to predict their behavior during the prediction horizon. Moreover, in smart grid applications, such a model is needed to simulate the microgrids behavior for at least one day ahead [10]. There are three major considerations that need to be taken into account when developing a mathematical model for the microgrids: i) the algebraic constraints presented by the PV module, wind turbine, and battery bank; ii) the battery bank as a subsystem with two modes of operation, namely, charging and discharging; and iii) the cycle life of the battery bank as a discontinuous differential state.

Algebraic constraints and bimodal operation of battery bank lead to a description of standalone dc microgrids as a set of hybrid differential algebraic equations (hybrid DAEs) [11, 12]. Therefore, the standalone dc microgrids can be represented by an acausal model for the control and simulation purposes. Unlike the causal approach, which requires the system being decomposed into a chain of causal interacting blocks consisting of only ordinary differential equations (ODEs), the acausal modeling is a declarative approach in which individual parts of the model are described as hybrid DAEs [12].

*Corresponding author
Email address:
arash.moradinegade@northumbria.ac.uk (Arash M. Dizqah)

Acausal modeling, as the mathematical representation of the system, is an effective way to model and simulate complex systems and such a model is also applicable to develop NMPC strategies. Modelica [13], as an object-oriented and equation-based language to describe complex systems, provides the capability to acausally model the class of hybrid dynamical systems [12].

Moreover, the cycle life of the batteries, as discontinuous differential states, cause the system to be of the non-Filippov type [14], which is more challenging to analyse. The cycle life is defined as the total number of complete charging/discharging cycles a battery can undergo before its capacity falls down below 80% of its nominal value. Apart from the cycle life, standalone dc microgrids can be modeled as differential inclusions (DIs) [15] of the Filippov type. The author in [16] argued that the NMPC strategies to control the hybrid systems of the Filippov type may be solved by employing a variable element length version of the collocation method. Applying this flexible version of the collocation method transfers such a NMPC problem into a mathematical programming with the complementarity constraints (MPCC). Then, employing the penalization method, the resulting MPCC can be transformed into a nonlinear programming (NLP) problem which can be solved by general purpose NLP solvers. However, in order to transform the NMPC problem to a MPCC, such problem should be of the complementarity class of the hybrid dynamical systems [17].

The main aim of this paper is to provide a mathematical model of the standalone dc microgrids applicable to NMPC strategies as well as long-term simulation purposes. For this aim the standalone dc microgrids are modeled as complementarity systems (CSs) including differential and algebraic constraints as well as mixed complementarity problems (MCPs). The discontinuous cycle life differential state is reformulated with a continuous approximation. Such a reformulation transforms the proposed dc microgrid model to be of the Filippov type. Moreover, the bimodal operation of the battery bank is also modeled as separate complementarity constraints. The developed model is then used in two different applications: i) the equivalent model in the form of DIs, is employed to simulate the standalone dc microgrids; and ii) a NMPC strategy based on the presented model is developed to track the load demands and regulate the dc bus voltage despite substantial generation fluctuations. It is shown that the developed model can be solved with DASSL general purpose DAE solver [18] equipped with the event detector and consistent re-initialization features. The obtained results indicate that the proposed model is accurate for simulating different variables of the dc microgrids using the OpenModelica environment [19]. Moreover, it is shown that the developed model is agile enough to be solved with available NLP solvers in order to be used in NMPC control strategies.

The remainder of this paper is organized as follows. Section 2 briefly describes the standalone dc microgrid studied in this paper. Section 3 provides preliminaries on mathematical concepts mentioned throughout the paper. Section 4 deals with the modeling of a standalone dc microgrid as a CS. Sections 5-6 present and discuss the above-mentioned two applications of the developed model of the standalone dc microgrids. Finally, the conclusion of the study is given in Section 7.

2. Standalone dc microgrids

Fig. 1 illustrates a topology of a standalone dc microgrid for the small-scale applications. It consists of wind, solar, and battery branches which are connected to the dc bus through dc-coupled structures, i.e. via dc-dc converters. The microgrid supplies a variable linear dc load which is connected directly to the grid bus.

The wind turbine operates at variable speeds and is connected to a permanent magnet synchronous generator (PMSG) directly, i.e. direct-drive coupling. The direct-drive coupling provides some advantages in terms of high reliability and is more popular for small-scale wind turbines [20]. In spite of high cost, the PMSG is the most dominant type of the direct-drive generators in the market [20], chiefly due to higher efficiency. The solar branch, in other hand, consists of a photovoltaic (PV) array that injects harvested energy into the microgrid through a boost-type converter. The authors in [21] showed that employing a dc-coupled structure to connect the battery bank to the dc bus is more flexible in terms of implementing different charging and discharging regimes and despite power losses.

From Fig. 1, it can be seen that the presented dc microgrid is controlled by four manipulated variables, i.e. the wind turbine pitch angle and the switching duty cycles of three different dc-dc converters. While increasing the wind turbine pitch
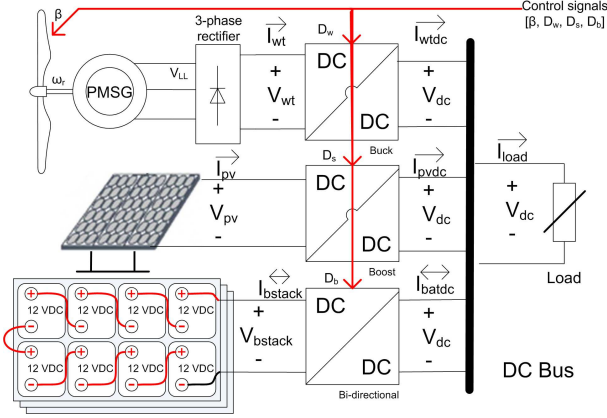
Fig. 1. The topology of a small-scale and standalone dc microgrid.

angle promotes pitching to feather, the operating points of the PMSG, PV, and battery bank can be changed by varying the dc-dc converters duty cycles.

3. Preliminaries

3.1. Introduction to the differential inclusions (DIs) of the Filippov type

Consider the following system:

$$\dot{\mathbf{x}} \in \boldsymbol{\mathcal{F}}(\mathbf{x}, \mathbf{u}; \mathbf{t}). \tag{1}$$

where $\mathcal{F}$ is a non-empty, bounded, and closed set of functions.

This piecewise continuous class of differential equations, which is known as differential inclusions [14], presents discontinuous right-hand sides. A differential inclusion given by Eq. (1) is of the Filippov type on an interval $[a, b]$ if the differential states remain continuous on that interval.

The following Eq. (2) indicates a specific representation of the differential inclusions with two modes of operation [16].

$$\dot{\mathbf{x}} = \begin{cases} f_-(\mathbf{x}, \mathbf{u}; \mathbf{t}) & \text{for} \quad \sigma(\mathbf{x}(\mathbf{t})) < 0, \\ \nu(t) f_-(\mathbf{x}, \mathbf{u}; \mathbf{t}) + \\ \quad (1 - \nu(t)) f_+(\mathbf{x}, \mathbf{u}; \mathbf{t}) & \text{for} \quad \sigma(\mathbf{x}(\mathbf{t})) = 0, \\ f_+(\mathbf{x}, \mathbf{u}; \mathbf{t}) & \text{for} \quad \sigma(\mathbf{x}(\mathbf{t})) > 0. \end{cases} \tag{2}$$

where $\mathbf{x}(\mathbf{t})$ and $\mathbf{u}(\mathbf{t})$ are the states and manipulated control signals, respectively. The switching function $\sigma(\mathbf{x}(\mathbf{t}))$ determines transitions between two modes of operation while a convex combination of the two models is allowed at the transition point with $\nu(t) \in [0, 1]$.

3.2. Introduction to complementarity systems (CSs)

CSs, as specific types of the class of hybrid dynamical systems, arise in several engineering applications dealing with multi-modal systems. A CS is formulated as the following general form which consists of orthogonal inequality (Eq. (3c)) also known as complementarity problem [17]:

$$0 = \boldsymbol{\mathcal{F}}(\mathbf{x}, \dot{\mathbf{x}}, \mathbf{u}, \boldsymbol{\gamma}; t), \tag{3a}$$

$$0 = \boldsymbol{\mathcal{G}}(\mathbf{x}, \mathbf{u}, \boldsymbol{\gamma}, \boldsymbol{\omega}; t), \tag{3b}$$

$$\boldsymbol{\mathcal{C}}^* \ni \boldsymbol{\omega} \perp \boldsymbol{\Gamma}(\boldsymbol{\gamma}) \in \boldsymbol{\mathcal{C}}, \tag{3c}$$

$$\mathbf{x}(\mathbf{t_0}) = \mathbf{x_0}. \tag{3d}$$

where $\perp$ is the complementarity operator indicating that at least one of the bounds is active. Let $\boldsymbol{\mathcal{C}}$ be a convex cone, then $\boldsymbol{\mathcal{C}}^*$ is the polar cone of $\boldsymbol{\mathcal{C}}$ defined as $\boldsymbol{\mathcal{C}}^* = \{\mathbf{z} | \mathbf{z^T}\nu \leq \mathbf{0}, \forall \nu \in \boldsymbol{\mathcal{C}}\}$. The slack variable $\boldsymbol{\gamma} \in \mathbb{R}^m$ and the signal $\boldsymbol{\omega} \in \mathbb{R}^m$ constitute a pair of complementarity variables and $\boldsymbol{\Gamma}(.)$ is some function.

Particularly, if one considers the convex cone $\boldsymbol{\mathcal{C}}$ as the interval $[\boldsymbol{\ell}, \mathbf{u}] \in \mathbb{R}_+$, then the complementarity problem given by Eq. (3c) is transformed to the class of mixed complementarity problems (MCPs) as follows:

$$0 = \boldsymbol{\mathcal{F}}(\mathbf{x}, \dot{\mathbf{x}}, \mathbf{u}, \boldsymbol{\gamma}; t), \tag{4a}$$

$$\boldsymbol{\ell} \leq \boldsymbol{\gamma} \leq \mathbf{u} \perp \boldsymbol{\Gamma}(\boldsymbol{\gamma}), \tag{4b}$$

$$\mathbf{x}(\mathbf{t_0}) = \mathbf{x_0}. \tag{4c}$$

where the function $\boldsymbol{\Gamma}(.)$ is multiplied with a negative sign to be a member of $\boldsymbol{\mathcal{C}}^*$ which is $-\mathbb{R}_+$. The complementarity problem given by Eq. (4b) has been simplified by considering the function $\boldsymbol{\mathcal{G}}$ as $\boldsymbol{\omega} - \boldsymbol{\gamma} = 0$.

Fig. 2 illustrates the solution of the MCP given by Eq. (4b). Such a solution is a vector $\boldsymbol{\gamma}$ such that for each function $\Gamma_i(.), i \in \{1, .., m\}$ one of the following cases holds:

$$\begin{cases} \gamma_i = \ell_i & \text{for} \quad \Gamma_i(\gamma) \geq 0, \\ \ell_i \leq \gamma_i \leq u_i & \text{for} \quad \Gamma_i(\gamma) = 0, \\ \gamma_i = u_i & \text{for} \quad \Gamma_i(\gamma) \leq 0. \end{cases} \tag{5}$$

As a result, the complementarity systems given by Eq. (4) has up to 2^m different modes of operation [17]. The authors in [16, 17] showed that the class of complementarity systems can be transformed to other classes of hybrid dynamical systems including DIs as well as the systems with equilibrium constraints.
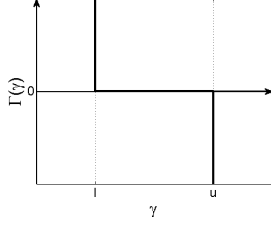
Fig. 2. The solution of the mixed complementarity problem $\mathcal{MCP}(\gamma, \Gamma)$.
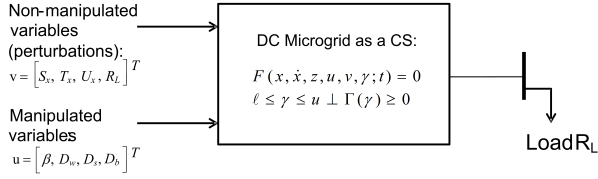

Fig. 3. The standalone dc microgrids as complementarity systems.

4. Model Development

The authors in [15] presented the mathematical model of the standalone hybrid wind and solar dc microgrids. Their model presents the dc microgrid as hybrid differential algebraic equations (hybrid DAEs) with differential inclusions. However, the challenging cycle life differential state, causing the system to be of the non-Filippov type, is not considered in their model. Moreover, the differential inclusions of the presented model in [15] should be converted to mixed complementarity problems in order to use such a model to develop model predictive control strategies.

Fig. 3 summarizes the developed model for the standalone dc microgrid given by Fig. 1. In Fig. 3, it can be seen that the dc microgrid is modeled as a CS including mixed complementarity problems with slack variables $\gamma = [\gamma_1, \gamma_2]^T$. Such a CS consists of differential and algebraic states, i.e. $\mathbf{x} = [\mathbf{I_f}, \mathbf{Q_{act}}, \omega_\mathbf{r}, \mathbf{V_{exp}}]^\mathbf{T}$ and $\mathbf{z} = [\mathbf{I_{pv}}, V_{pv}, I_{pvdc}, I_{bstack}, V_{bstack}, I_{batdc}, I_{wr}, V_{wr}, I_{wtdc}, T_e, T_m, \lambda, C_p, SOC, I_{load}, V_{dc}]^T$, and manipulated and non-manipulated control variables, namely, $\mathbf{u}$ and $\mathbf{v}$, which are detailed later throughout the next subsections.

In what follows, the following notations are used to model the standalone dc microgrid depicted in Fig. 1 as a CS given by Eq. (4):

$$\mathcal{F}(\mathbf{x}, \dot{\mathbf{x}}, \mathbf{z}, \mathbf{u}, \mathbf{v}, \boldsymbol{\gamma}) = \left[\begin{array}{c} f_1(\mathbf{x}, \dot{\mathbf{x}}, \mathbf{z}, \mathbf{u}, \mathbf{v}, \boldsymbol{\gamma}) \\ f_2(\mathbf{x}, \dot{\mathbf{x}}, \mathbf{z}, \mathbf{u}, \mathbf{v}, \boldsymbol{\gamma}) \\ .. \\ f_{25}(\mathbf{x}, \dot{\mathbf{x}}, \mathbf{z}, \mathbf{u}, \mathbf{v}, \boldsymbol{\gamma}) \end{array} \right] = 0, \tag{6a}$$

$$\mathcal{MCP}(\boldsymbol{\gamma}, \boldsymbol{\Gamma}) = \left[\begin{array}{c} \mathcal{MCP}_1(\gamma_1, \Gamma_1(\mathbf{x}, \mathbf{z}, \gamma_1)) \\ \mathcal{MCP}_2(\gamma_2, \Gamma_2(\mathbf{x}, \mathbf{z}, \gamma_2)) \end{array} \right]. \tag{6b}$$

where $\mathcal{F}$ is a set of implicit differential and algebraic functionals f_i for $i \in \{1, 2, .., 25\}$ that models the dc microgrids behaviors. All the equations that are not indicated as implicit functions $\{f_i\}$ are used to calculate intermediate variables. $\mathcal{MCP}$ is a vector of two MCPs as in Eq. (4b) that models the different modes of operation and any transitions between them.

The following sub-sections present all the differential and algebraic equations that model the battery, solar, and wind branches. Connecting all these branches together, there are two power balance constraints given by algebraic Eq. (7) indicate that the sum of the generation and the consumption powers should always be zero.

$$f_1 = V_{dc}\Big(I_{pvdc} + I_{wtdc} + I_{batdc} - I_{load}\Big), \tag{7a}$$

$$f_2 = V_{dc} - I_{load}R_L. \tag{7b}$$

4.1. The battery branch

The authors in [22] introduced a model to mathematically represent the lead-acid battery. This model can be generalized as a CS by introducing the following MCP:

$$\mathcal{MCP}_1 : 0 \leq \gamma_1 \leq 1 \quad \perp \quad \Gamma_1(\mathbf{x}, \mathbf{z}, \gamma_1) = \mathbf{I_{bstack}}, \tag{8}$$

where I_{bstack} is the current of a battery stack. Regarding the solution of a MCP given by Eq. (5), γ_1 is a slack variable indicates if the battery bank operates either in the charging ($\gamma_1 = 1$) or discharging ($\gamma_1 = 0$) mode of operation. It is important to note that according to the notation throughout this paper, I_{bstack} is negative during the charging mode of operation.

Therefore, a lead-acid battery bank, consisting of N_{batp} battery stacks in parallel and each stack consists of N_{bats} batteries in series, can be modeled as the following DAEs coupled with the complementarity constraint given by Eq. (8). It is important

to note that at every instant only one of the segments of the equations is active in terms of the value of γ_1:

$$f_3 = \frac{V_{bstack}}{N_{bats}}+$$
$$\gamma_1 \left\{ R_{bat}\frac{I_{bstack}}{N_{batp}} - V_0 + \frac{P_1 C_{max}}{C_{max}-Q_{act}}Q_{act}+ \right.$$
$$\left. \frac{P_1 C_{max}}{0.1 C_{max}+Q_{act}}I_f - V_{exp} \right\}+$$
$$(1-\gamma_1)\left\{ R_{bat}\frac{I_{bstack}}{N_{batp}} - V_0 + \frac{P_1 C_{max}}{C_{max}-Q_{act}}Q_{act}+ \right.$$
$$\left. \frac{P_1 C_{max}}{C_{max}-Q_{act}}I_f - V_{exp} \right\}. \tag{9a}$$

$$f_4 = \frac{dQ_{act}}{dt}(t) - \frac{1}{3600}\frac{I_{bstack}(t)}{N_{batp}}, \tag{9b}$$

$$f_5 = \frac{dI_f}{dt}(t) + \frac{1}{T_s}(I_f - \frac{I_{bstack}}{N_{batp}}), \tag{9c}$$

$$f_6 = \frac{dV_{exp}}{dt}(t) - \gamma_1\left\{ \frac{P_2}{3600}\left|\frac{I_{bstack}}{N_{bats}}\right|(P_3 - V_{exp}) \right\}+$$
$$(1-\gamma_1)\left\{ \frac{P_2}{3600}\left|\frac{I_{bstack}}{N_{bats}}\right|V_{exp} \right\}, \tag{9d}$$

$$f_7 = V_{bstack} - \frac{V_{dc}}{1-D_b}, \tag{9e}$$

$$f_8 = I_{bstack} - (1-D_b)I_{batdc}, \tag{9f}$$

$$f_9 = SOC - \left\{ 1 - \frac{Q_{act}}{C_{max}} \right\}. \tag{9g}$$

V_{bstack}, I_{bstack} and SOC, respectively, are the voltage, current, and the state of charge of the battery stack. The parameters $P_1 - P_3$ are experimental require being identified for each type of the battery. The C_{max} is the maximum amount of the battery capacity, R_{bat} is the internal resistor of the battery, Q_{act} is the actual battery capacity, and V_0 is the battery constant voltage. Moreover, I_f is the filtered value of the battery current with the time constant of T_s [22]. The bi-directional converter with the duty cycle D_b of the boost switching power pole is modeled in steady-state continuous conduction mode (CCM) [23].

The cycle life of a battery bank, as a measure to calculate the cost of its delivered energy [24], mainly depends on two factors: the number of charging/discharging cycles and the depth of each discharge. Fig. 4a illustrates the normalized cycle life that is a discontinuous differential state being increased by the reverse of equivalent full cycle (EFC) at the moment of each mode switching from
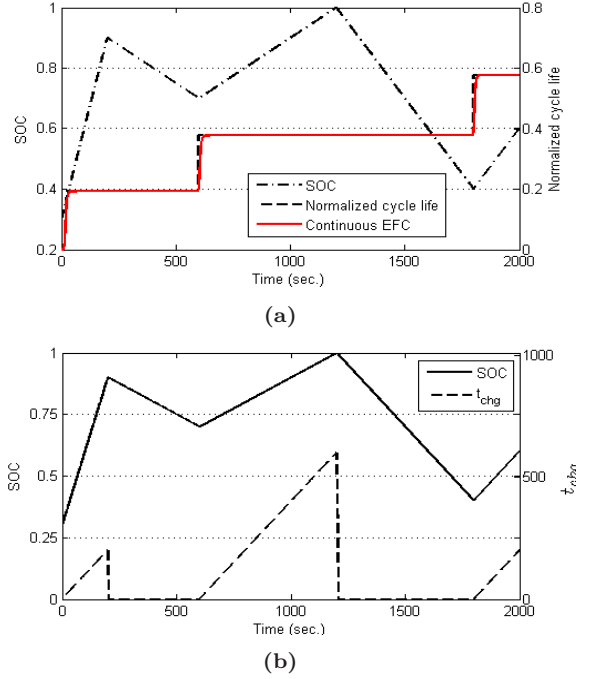

Fig. 4. (a) Discontinuous cycle life differential state and its equivalent continuous approximation; and (b) the introduced charging cycle, t_{chg}, state of the battery and the relevant SOC variations.

discharging to charging. EFC indicates the number of cycles of a battery at any depth of discharge (DOD) which is given by a curve for different values of DOD [24].

In order to model cycle life as a continuous differential state and therefore convert the system to the class of the Filippov type, a new continuous state, t_{chg}, is defined as given by Fig. 4b which indicates the duration of the charging cycle. The t_{chg} starts from zero and monotonically increases during the charging cycle. Once the battery switches to discharging mode, t_{chg} sharply drops down to zero. Such a differential state can be defined using the following complementarity problem:

$$\mathcal{MCP}_2 : 0 \leq \gamma_2 \leq 1 \quad \perp \quad \Gamma_2(\mathbf{x}, \mathbf{z}, \gamma_2) = -\mathbf{t_{chg}}, \tag{10}$$

where γ_2 is a slack variable shows that if t_{chg} is positive then $\gamma_2 = 1$, otherwise $\gamma_2 = 0$.

Having the complementarity constraints given by Eq. (10), one can model the t_{chg} as the following differential inclusion:

$$f_{10} = \frac{\mathrm{d}t_{chg}}{\mathrm{d}t}(t) - \left(\gamma_1 - 1000(1 - \gamma_1)\right)\gamma_2. \quad (11)$$

Eqs. (10) and (11) show that when $t_{chg} \geq 0$, its value increases with the unity rate if battery is in charging mode, i.e. $\gamma_1 = 1$. Once the battery switches to the discharging mode, i.e. $\gamma_1 = 0$, the value of the t_{chg} falls down with the rate of -1000 until t_{chg} reaches zero when it remains constant afterward. Given Eq. (11), one can use Eq. (12) to model the cycle life, $cycle_L$, as a continuous differential state. It is based on the fact that the cycle life equals to $\sum_{n=1}^{\infty} \frac{1}{EFC(DOD_n)}$, where n is the number of discharging to charging mode switches and EFC depends on the value of the $DOD_n = 1 - SOC_n$ at which the battery switches to the charging mode. Fig. 4a illustrates the resulting continuous cycle life comparing with the original discontinuous value. In Fig. 4a, it can be seen that the value of cycle life becomes steady a little while after switching to charging mode, i.e. $t_{chg} \cong 20$, or during discharging mode, i.e. $\gamma_1 = 0$.

$$f_{11} = \frac{\mathrm{d}cycle_L}{\mathrm{d}t}(t) - \gamma_1 exp(-t_{chg})$$
$$\underbrace{\left\{ \left(1 - SOC\right) \underbrace{\frac{1159SOC^2 - 952SOC + 745.3}{-SOC + 1.05909}}_{\text{Number of cycles}} \right\}^{-1}}_{\text{Equivalent full cycle}}. \quad (12)$$

4.2. The solar branch

The authors in [25] presented a mathematical model of the solar branch, consisting of a PV array that is connected to the dc bus through a boost-type dc-dc converter. The presented model is based on the equivalent electrical circuit of the PV module [26, 27] as well as the average model of the connected dc-dc converter [23]. The average model of the converter can be replaced with the following steady-state equations in CCM:

$$f_{12} = V_{pv} - (1 - D_s)V_{dc}, \quad (13a)$$
$$f_{13} = I_{pvdc} - (1 - D_s)I_{pv}. \quad (13b)$$

A PV array consists of, respectively, N_{pvs} and N_{pvp} PV modules in series and parallel. Given the photocurrent, I_{ph}, and diode reverse saturation current, I_0, as Eqs. (14b) and (14c), one can model

a PV array with the transcendental characteristic equation given by Eq. (14a) [27].

$$f_{14} = I_{pv} - I_{ph} + \frac{V_{pv} + \frac{N_{pvs}}{N_{pvp}}R_s I_{pv}}{\frac{N_{pvs}}{N_{pvp}}R_{sh}} +$$
$$I_0 \left\{ exp(\frac{V_{pv} + \frac{N_{pvs}}{N_{pvp}}R_s I_{pv}}{n_d N_s}\frac{q \times N_{pvs}}{KT_c}) - 1 \right\}, \quad (14a)$$

$$f_{15} = I_{ph} - N_{pvp} \times$$
$$\left(\frac{R_s + R_{sh}}{R_{sh}}I_{sc,stc} + k_I\left(T_c - T_{c,stc}\right) \right)\frac{S}{S_{stc}}, \quad (14b)$$

$$f_{16} = I_0 - N_{pvp} \times$$
$$\frac{I_{sc,stc} + k_I\left(T_c - T_{c,stc}\right)}{exp(\frac{V_{oc,stc} + k_V\left(T_c - T_{c,stc}\right)}{n_d N_s}\frac{q}{KT_c}) - 1}. \quad (14c)$$

where R_s and R_{sh}, respectively, are the series and parallel equivalent resistors of the PV module and all other parameters are as follows:

q	Electron charge (1.60218×10^{-19})
N_s	The number of the PV cells in PV module (-)
K	Boltzman constant (1.38066×10^{-23})
k_I	Short-circuit current temperature coefficient (A/C)
T_c	The current PV cell temperature (K)
$I_{sc,stc}$	Short-circuit current at the STC (A)
S	The current solar irradiance (W/m)
k_V	Open-circuit voltage temperature coefficient (V/C)
S_{stc}	S Insolation level (W/m)
$T_{c,stc}$	STC cell temperature (K)
$V_{oc,stc}$	Open-circuit voltage at the STC (V)

4.3. The wind branch

The wind turbine performance can be measured according to the power coefficient curve, C_p, [28] with respect to the tip speed ratio, λ (Eq. 15a)), and the pitch angle β. Eq. (15c) gives the C_p curve of a wind turbine [29] consisting of three blades with radius, Rad, of 4.01 meter. Such a wind turbine generates the maximum power coefficient of 0.48 at the optimum tip speed ratio of 8.1.

$$f_{17} = \lambda - \frac{Rad \times \omega_r}{U_x}, \quad (15a)$$

$$f_{18} = \lambda_i - (\frac{1}{\lambda + 0.08\beta} - \frac{0.035}{\beta^3 + 1})^{-1}, \quad (15b)$$

$$f_{19} = C_{p,norm} - \frac{1}{C_{p,max}}(C_1(\frac{C_2}{\lambda_i} - C_3\beta - C_4)$$
$$exp(-\frac{C_5}{\lambda_i}) + C_6\lambda). \quad (15c)$$

The experimental coefficients $C_1 - C_6$ are defined in Table 2. λ_i in Eq. (15b) is an intermediate variable to make the equations easier to understand.

All fast voltage and current dynamics, except the angular velocity of the generator given by Eq. (16a), can be ignored for the long-term simulation and outer controller applications. For the sake of simplicity, it is assumed that there is no mechanical and electrical losses through the powertrain. Therefore, the electromagnetic power given by Eq. (16b) is equal to the output electrical power of the wind branch.

$$f_{20} = \frac{\mathrm{d}\omega_r}{\mathrm{d}t}(t) - \frac{1}{J}(T_e - T_m - F\omega_r), \tag{16a}$$

$$f_{21} = -T_e \times \omega_r - I_{wtdc} \times V_{dc}, \tag{16b}$$

$$f_{22} = -T_m \times \omega_r - C_{p,norm}\left(\frac{U_x}{U_{x,base}}\right)^3 P_{nom}, \tag{16c}$$

$$V_{LL} = \frac{1}{\sqrt{2}} k_E \omega_r, \tag{16d}$$

$$k_E = \sqrt{3}P\psi. \tag{16e}$$

The shaft inertia J $(Kg.m^2)$ and the combined viscous friction coefficient F $(N.m.s)$ of the PMSG are given by the manufacturers. The V_{LL}, i.e. the r.m.s. value of the line-to-line output voltage of the generator given by Eq. (16d), depends on the mechanical angular velocity. Having the number of the pole pairs P and the flux linkage ψ $(V.s)$ (see Table 2), one can use Eqs. (16d) and (16e) to calculate the r.m.s. value of the line-to-line output voltage, V_{LL}, and the voltage constant k_E of the generator.

Similar to the battery and solar branches, the buck converter can be modeled in steady-state CCM:

$$f_{23} = V_{dc} - D_w V_{wt}, \tag{17a}$$

$$f_{24} = I_{wt} - D_w I_{wtdc}. \tag{17b}$$

where D_w is the switching duty cycle of the converter and all remaining parameters are as in Fig. 1.

The average dc output voltage of the rectifier, V_{wt}, in presence of the non-instantaneous current commutation is calculated as follows [23]:

$$V_{wt} = 1.35 V_{LL} - \frac{3}{\pi} P \omega_r L_s I_{wt}, \tag{18}$$

Replacing Eqs. (16d), (16e), and (17) into Eq. (18) and rearranging, one has the following equation to calculate the dc output current of the wind branch, I_{wtdc}:

$$f_{25} = I_{wtdc} - \frac{\pi}{3P\omega_r L_s D_w}\left\{\frac{1.35\sqrt{3}P\psi\omega_r}{\sqrt{2}} - \frac{V_{dc}}{D_w}\right\}. \tag{19}$$

5. Application I: Long-term simulation of the standalone dc microgrids

5.1. Modelica model of the standalone dc microgrid

In order to simulate the standalone dc microgrid given by Fig. 1, the presented mathematical model given by Eq. (6) is declared with Modelica modeling language [13]. The OpenModelica platform [19], including a Modelica compiler and DASSL [18] general purpose DAE solver, is selected to simulate the system chiefly because it is an open-source software and it supports more features of the Modelica language comparing with others. Table 1 summarizes the developed Modelica model. In Table 1, the MCPs given in Eqs. (8) and (10) are indicated by symbol †. They are translated into IF-THEN-ELSE Modelica propositions. Moreover, DIs given in Eqs. (9a), (9d), and (11), marked with symbol ‡, are also translated into IF-THEN-ELSE propositions. It is important to note that the model is of the Filippov type and therefore there is no need to re-initialize any state variable after mode switching.

5.2. Simulation results

The proposed Modelica model is used to simulate a sample standalone dc microgrid consisting of an array of the Kyocera KC200GT PV modules, a bank of the Panasonic LC-R127R2PG lead-acid batteries, and a wind branch. The authors in [22, 27, 29] presented the identified electrical parameters of the employed lead-acid battery, PV module, and wind turbine. Table 2 summarizes all parameters and their values in this study.

Fig. 5a compares the simulated current-voltage $(I - V)$ curve of the KC200GT PV module at the STC condition with the experimental curve available by the manufacturer in datasheet (the circle markers). It is observed that the proposed model predicts the curve very close to the empirical data provided by the manufacturer.

7

Table 1
Outline of the developed Modelica model. MCPs and DIs are respectively indicated by † and ‡.

---

class HRES

...;
discrete Boolean gamma1 "true: charging";
Real soc(start = 0.6, fixed = true) "State of charge of the battery";
Real tchg "The period of time that the battery is in charging state";
RealInput Ux "The wind speed (m/s)";
RealInput beta "The pitch angle (degree)";
RealInput Dw "The buck converter duty-cycle [0,1]";

equation

$Ipv = Iph - I0*(exp((Ipv*rs\_Tc + Vpv)/a\_Tc) - 1) - (Ipv*rs\_Tc + Vpv)/rsh\_Tc\_Sx;$
$Iph = (Npvp*((Rsh + Rs)/Rsh*Isc\_stc + Ki*(Tc - Tc\_stc))*Sx)/Sx\_stc;$
$I0 = (Npvp*(Isc\_stc + Ki*(Tc - Tc\_stc)))/(exp(((Voc\_stc + Kv*(Tc - Tc\_stc))*q)/(nD*Ns*K*Tc)) - 1);$
$Vpv = Vdc*(1 - Ds);$
$Ipvdc = (1 - Ds)*iPV;$
$gamma1 = \textbf{if } Ibstack \le 0 \textbf{ then true else false}; \quad (†)$
$der(If) = -1/Ts*If + Ibstack/(Ts*Nbatp);$
$der(Qact) = 1/3600*Ibat;$
$der(Vexp) = \textbf{if } gamma1 \textbf{ then } P2/3600*abs(Ibstack/Nbatp)*(P3 - Vexp) \textbf{ else } -(P2*abs(Ibstack/Nbatp))/3600*Vexp; \quad (‡)$
$soc = 1 - Qact/Cmax;$
$Vbstack/Nbats = \textbf{if } gamma1 \textbf{ then } (‡)$
  $V0 - R*Ibstack/Nbatp - (P1*Cmax)/(Cmax - Qact)*Qact - (P1*Cmax)/(Qact + 0.1*Cmax)*If + Vexp$
  $\textbf{else } V0 - R*Ibstack/Nbatp - (P1*Cmax)/(Cmax - Qact)*Qact - (P1*Cmax)/(Cmax - Qact)*If + Vexp;$
$der(tchg) = \textbf{if } gamma1 \textbf{ then } 1 \textbf{ elseif } tchg > 0 \textbf{ then } -1000 \textbf{ else } 0; \quad (†‡)$
$der(cycleL) = \textbf{if } gamma1 \textbf{ then } 100/((1 - soc)*(1159*soc \verb|^| 2 - 952*soc + 745.3)/(-soc + 1.05909))*exp(-tchg)$
  $\textbf{else } 0; \quad (‡);$
$-Te*\omega r = Iwtdc*Vbstack;$
$Ibstack = Ibatdc*(1 - Db);$
$Vbstack = Vdc/(1 - Db);$
$-Tm*\omega r = Cp\_pu*(Ux/12)\verb|^|3*Pnom;$
$der(\omega r) = (Te - Tm - F*\omega r)/J;$
$Iwtdc = pi*(1.35*P*psi*sqrt(3)*\omega r)/sqrt(2)/(3*Lst*P*\omega r*Dw);$
$lambda = (R*\omega r)/Ux;$
$lambda\_i = 1/(1/(lambda + 0.08*beta) - 0.035/(beta\verb|^|3 + 1));$
$Cp = (C1*(C2/lambda\_i - C3*beta - C4)*exp(-C5/lambda\_i) + C6*lambda)/0.48;$
$Vdc = Iload*RL;$
$Ipvdc + Ibatdc + Iwtdc = Iload;$

end HRES;

Table 2
The wind turbine, PMSG, battery stack, and PV parameters in this study.

| Wind turbine		PMSG		Battery stack		PV array	
$C_1(-)$	0.517	$J(Kg.m^2)$	0.35	$C_{max}(Ah)$	48.15	$R_s(\Omega)$	0.221
$C_2(-)$	116.0	$F(N.m.s)$	0.002	$R_{bat}(\Omega)$	0.019	$R_{sh}(\Omega)$	405.4
$C_3(-)$	0.4	$P(-)$	8	$V_0(V)$	12.3024	$n_d(-)$	1.3
$C_4(-)$	5.0	$\psi(V.s)$	0.8	$P_1(-)$	0.9	$N_s(-)$	54
$C_5(-)$	21.0	$P_{rated}(KW)$	10.0	$N_{bats}(-)$	8	$I_{sc,stc}(A)$	8.21
$C_6(-)$	0.007	$L_s(H)$	0.0083	$N_{batp}(-)$	3	$V_{oc,stc}(V)$	32.9
$\lambda_{opt}(-)$	8.1			$T_s(sec)$	0.726	$k_I(A/K)$	0.003
$P_{wt,nom}(KW)$	10.0			$V_{bstack,nom}(V)$	96.0	$k_V(V/K)$	-0.12
Rad (m)	4.01			$P_{bat,nom}(KW)$	1.296	$N_{pvs}(-)$	1
$U_{x,base}(m/s)$	12.0			$C_{10}(Ah)$	45.0	$N_{pvp}(-)$	10
$C_{p,max}(-)$	0.48			$V_{gas}(V)$	13.0	$P_{pv,nom}(KW)$	2.001
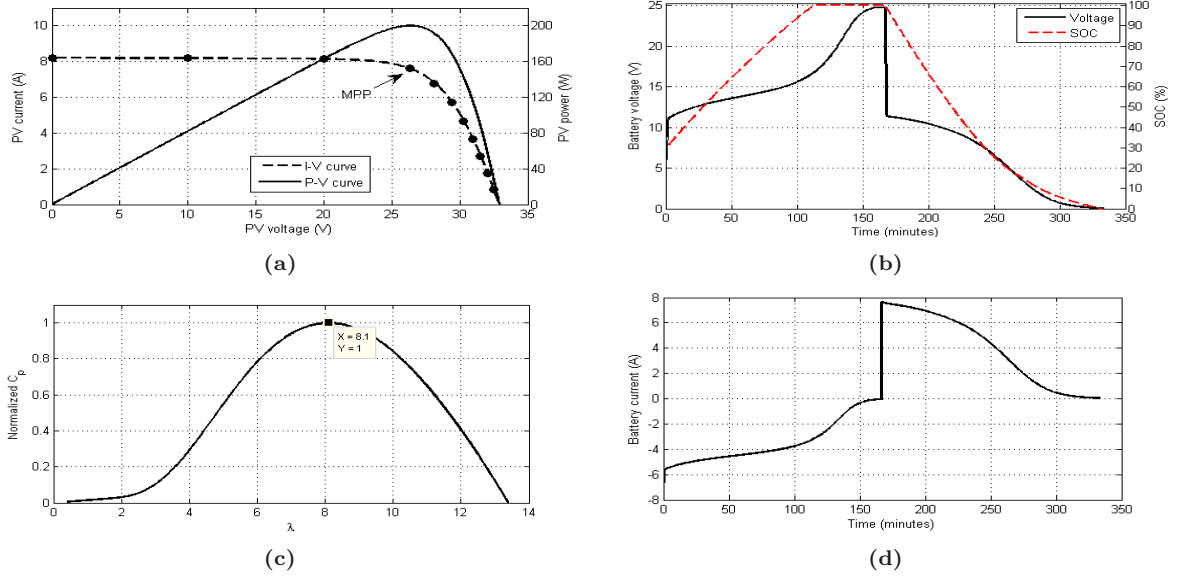
Fig. 5. (a) The simulated $I - V$ (dashed line) and $P - V$ (solid line) curves against the experimental points (the circle markers) of the KC200GT PV module; the simulated (b) voltage and (d) current of the battery; and (c) the simulated power coefficient curve of the wind turbine.

The simulation results of a single LC-R127R2PG lead-acid battery for a full operating cycle including charging, over-charging, saturation, discharging, over-discharging, and exhaustion zones are given by Figs. 5b and 5d. While the battery is being charged for around 160 minutes, it is discharged afterward. It also indicates that after 80 minutes it enters into the over-charging zone. Battery is fully charged at 112 minutes and the sunken current afterwards is totally dissipated in the form of heat or water electrolysis. Discharging with the current of $7.2A$ in average, it takes around 35 minutes for the battery, which matches with the information available in datasheet, to reach the cut-off voltage that is around $10.2V$.

Fig. 5c illustrates the results obtained from the wind turbine simulation. In Fig. 5c, it can be seen that the wind turbine generates the maximum lift at $\lambda_{opt} = 8.1$ which is matched with characteristics of the employed wind turbine [29].

The following test scenario is carried out to evaluate the stability of the developed model by applying different step changes to the manipulated and non-manipulated variables:

- After 100 seconds the load demand sharply changes from 65% to 20% of the maximum value.

- There is a step change in wind speed at time 350 seconds from 100% to 167% of the rated speed.

- At $t = 300$ seconds, insolation falls to 50% from the initial 100% of the maximum level.

- The wind turbine pitch angle and the wind branch duty cycles change to perform pitch control at $t = 350$ seconds and to remove the wind branch generations between $t = 500$ and 600 seconds.

Fig. 6a illustrates the manipulated variables that harvest the maximum power of the solar and wind branches (Fig. 6b), i.e. $2KW$ and $10KW$ respectively. In Fig. 6a, it can be seen that at $t = 350$ seconds, when the wind speed increases by 67%, the pitch angle goes up to 20 degrees and promotes pitching to feather [28]. In effect, although the wind speed reaches to 67% above the rated value, the generated power by the wind turbine remains stable at the rated value, i.e. $10KW$. Moreover, in Fig. 6c, it can be seen that despite an initial sharp increase causing by one second of the pitch controller delay, the rotational speed of the wind turbine returns back. Fig. 6a and 6b show that a sharp decrease of D_w at $t = 500$ seconds makes the wind turbine share of the electrical power to become zero between $t = 500$ and 600 seconds.
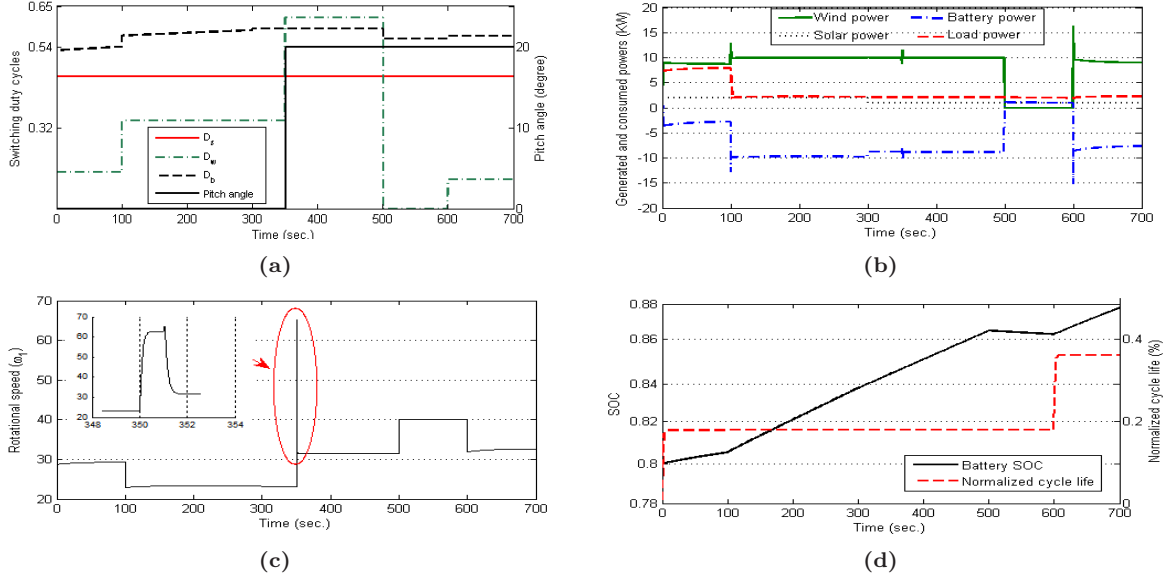
9

Fig. 6. Applied (a) switching duty cycles and pitch angle values for the simulation purposes; and the simulation results for the (b) electrical current of each branch, (c) angular velocity of the wind turbine; and (d) cycle life as well as SOC of the battery bank.

Any discharging to charging mode transitions increase the cycle life of the battery by $\frac{1}{EFC(DOD_n)}$ as given by Fig. 6d. From Fig. 6d, it can be seen that the cycle life, as an inherently discontinuous state, is modeled with a continuous approximation. Battery starts absorbing the excess of energy from the beginning and the absorbing rate increases at $t = 100$ seconds after a substantial reduction in load demand. It also compensates the energy deficit of the system during the period of time between $t = 500$ and $t = 600$ seconds when the wind branch is removed.

6. Application II: NMPC-based multivariable load tracking strategy for standalone dc microgrids

This section presents a brief description on the optimal control theory and NMPC, as the employed control strategy, followed by the control system design. For further details on NMPC, the reader is referred to [6, 7, 30].

6.1. Introduction to the nonlinear mode predictive control (NMPC)

NMPC strategies make explicit use of the system model, given by $\mathcal{F}$, in order to find an optimal control law $u^*(.)$ while maintaining a set of equality

and inequality constraints [7]. The term optimal here is defined with respect to the cost functional J that consists of the Lagrangian term $\mathcal{L}$, which is the sum of the deviations within the period of time T, as well as the terminal penalty term $\mathcal{M}$, as the deviations from the final values. A NMPC strategy iteratively solves an optimal control problem (OCP), given in Eq. (20), at time t and apply the first optimal value as the next control signal [6]. Eqs. (20d)) and (20e)), respectively, represents initial and final constraints and Eq. (20g) models the boxing constraints that should be maintained by the optimal solution. Comparing with the conventional methods, NMPC strategies are inherently nonlinear and multivariable that handle constraints and delays [30].

$$\mathbf{u}^*(.) = \arg\min_{\mathbf{u}(.) \in \mathcal{U}^N} J_N(\mathbf{x}, \mathbf{z}, \mathbf{u}; n) :=$$

$$\sum_{k=n}^{n+N-1} \mathcal{L}(\mathbf{x}(k), \mathbf{z}(k), \mathbf{u}(k))$$

$$+ \mathcal{M}(\mathbf{x}(n+N), \mathbf{z}(n+N)) \quad (20a)$$

subject to:

$$\mathcal{F}(\mathbf{x}(k), \dot{\mathbf{x}}(k), \mathbf{z}(k), \mathbf{u}(k), \mathbf{v}(k)) = 0 \quad (20b)$$

$$\mathcal{H}(\mathbf{x}(k), \mathbf{z}(k), \mathbf{u}(k)) \leq 0 \quad (20c)$$

$$\mathbf{x}(n) = \mathbf{x}_0, \mathbf{z}(n) = \mathbf{z}_0 \quad (20d)$$

$$\mathcal{R}(\mathbf{x}(n+N), \mathbf{z}(n+N)) = 0 \quad (20e)$$

$$\forall k \in [n, n+N-1] \quad (20f)$$

$$\mathbf{x}(k) \in \mathcal{X}, \mathbf{z}(k) \in \mathcal{Z}, \mathbf{u}(k) \in \mathcal{U}. \quad (20g)$$

Conventionally some specific forms of Eq. (20) can be solved with the dynamic programming and indirect methods. In order to solve more general forms of Eq. (20), there are recently developed direct methods [6]. The direct methods discretize involved OCP, by for instance the collocation method, and convert it into a nonlinear optimization problem (NLP) that can be solved by general purpose NLP solvers [6, 16].

6.2. Controller design

Due to substantial generation and demand fluctuations in standalone dc microgrids, energy management strategies (EMSs) are becoming essential for regulating the microgrid voltage and tracking the load demands. As an application of the developed standalone dc microgrids model, a NMPC-based realization of EMS is proposed. The proposed controller employs the collocation method for discretization [16] and is implemented in open-source CasADi environment [31] to benefit from the automatic differentiation (AD) technique and improve performances [31].

As given in Eqs. (6a) and (6b), the set of functionals $\{f_1, .., f_{25}\}$ and $\{\mathcal{MCP}_1, \mathcal{MCP}_2\}$ construct the system model $\mathcal{F}$ of the involved OCP. Due to existent MCPs in the system model, the resulting OCP is of the class of mathematical programming with complementarity constraints (MPCC) problems [16]. In order to use ordinary NLP solvers, the MCPs given in Eqs. (8) and (10) can be regularized as the following equality and inequality constraints [16]:

$$\mathbf{\Gamma}(\boldsymbol{\gamma}) - \mathbf{w} + \mathbf{v} = \mathbf{0},$$

$$\mathbf{w}, \mathbf{v} \geq \mathbf{0}, \quad \mathbf{w}^\mathbf{T}\boldsymbol{\gamma} = \epsilon, \quad \mathbf{v}^\mathbf{T}(\mathbf{1} - \boldsymbol{\gamma}) = \epsilon. \quad (21)$$

where $0 < \epsilon \ll 1$ is a design parameter and $\mathbf{\Gamma}(\boldsymbol{\gamma}) = [\Gamma_1(\gamma_1) \quad \Gamma_2(\gamma_2)]^T = [I_{bstack} \quad - t_{chg}]^T$ and $\boldsymbol{\gamma} = [\gamma_1 \quad \gamma_2]^T$ are respectively the functions and slack variables given in Eqs. (8) and (10). Moreover, $\mathbf{w} = [w_1 \quad w_2]^\mathbf{T}$ and $\mathbf{v} = [v_1 \quad v_2]^\mathbf{T}$ are new defined slack variables.

6.2.1. Control objectives

The developed energy management strategy in this paper addresses two control objectives: i) maximizing the battery bank SOC; and ii) regulating the dc bus voltage level of the microgrid. These objectives are formulated as the cost function J and a path constraint h_1, respectively, because while the former should be as close to one as possible, the latter, which is the stability indicator of microgrid, must always be within a permissible range.

The cost function J, given in Eq. (22), is the battery bank deviation from the fully charged status which should be minimized with respect to the manipulated control signals $\mathbf{u}$ and slack variables $\mathbf{w}$, $\mathbf{v}$, and $\boldsymbol{\gamma}$.

$$J_N(\mathbf{x}, \mathbf{z}, \mathbf{u}; n) :=$$

$$\sum_{k=n}^{n+N-1} \|SOC(k) - 1.0\|_2 + \|SOC(n+N) - 1.0\|_2. \quad (22)$$

The permissible deviation of the dc bus voltage level V_{dc} from the specified set point $\overline{V}_{dc}$ is given in Eq. (23) as a slack variable α_1 which is a design parameter.

$$h_1: \quad |V_{dc} - \overline{V}_{dc}| - \alpha_1 \leq 0. \quad (23)$$

In this study, the design parameter α_1 is set to be in the range of $\pm 2\%$ of the $\overline{V}_{dc}$. It means that for the set point of 48.0 volt, the maximum permissible deviation is ± 0.96 volt.

6.2.2. Control constraints

The generated power by the wind turbine is limited to the rated power by employing a pitch angle controller [28]. This requirement is addressed by the following path constraint:

$$h_2: \quad -T_e\omega_r - P_{wt,nom} \leq 0. \quad (24)$$

The variation of the wind turbine angular velocity, i.e. $\Delta(\omega_r)$, is also limited in order to decrease the tower vibrations [28]. Moreover, SOC of the battery bank must be within a permissible range, e.g. [0.60, 0.90]. The charging and discharging currents of each member of the battery bank are also

Parameter Name	Value
Prediction horizon T (sec)	60
Sampling time h (sec)	12.0
No. of the discretization samples N	5
$\overline{V}_{dc}(V)$	48.0
Average Computational Time (sec)	5.97
Minimum Computational Time (sec)	1.98
Maximum Computational Time (sec)	13.81

limited to $0.16C_{10}$ and $0.23C_{10}$ amperes, respectively, where C_{10} is the nominal capacity of each battery given in Table 2.

6.3. Results and discussion

The performance of the developed optimal load tracker strategy in terms of different control objectives is evaluated by carrying out a test scenario. In order to solve the resulting OCP with a general purpose NLP solver, it is assumed that the battery bank only switches between the charging and discharging modes of operation at the edge of the discretized time slots.

Table 3 summarizes the design parameters and performance indicators of the developed NMPC controller. The computational times are calculated on an Intel CORE 2 DOU machine with $3GB$ of RAM. The microgrids' states are evaluated every sampling time $h= 12$ seconds. The developed solver computes optimal pitch angle and switching duty cycles in average within 5.97 seconds which is very close to the 5 seconds evaluation time criterion specified by the hierarchical architecture specifications [32]. The optimal pitch angle, $\bar{\beta}$, is applied as a set point to an inner closed-loop controller. Moreover, the optimal values of the switching duty cycles are applied to the pulse width modulators (PWMs) of the dc-dc converters.

The non-manipulated variables, i.e. the wind speed, insolation, and load demand, are applied to the system according to the given profiles in Fig 7a. Fig 7b illustrates the calculated optimal pitch angle and one of the switching duty cycles, i.e. D_w. Pitch angle is increased between 60 to 180 seconds when wind speed rises substantially. The wind turbine rotational speed is also decreased down to $21.7(rad/s)$, as in Fig. 7c. In response, the normalized power coefficient of the wind turbine in Fig. 7c is declined to 0.630 and then to 0.393. Fig. 7d shows that despite a wind speed increase of 38%, the wind branch power remains steady at its
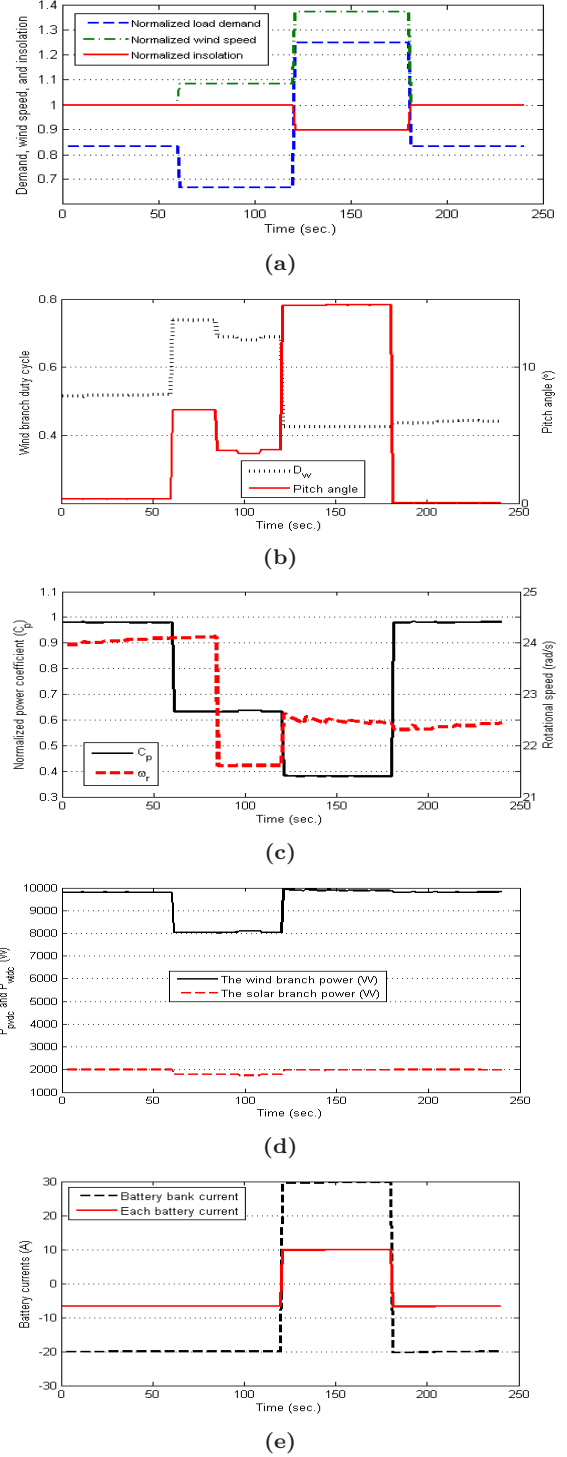

(a)

(b)

(c)

(d)

(e)

Fig. 7. The (a) normalized values of the applied non-manipulated variables; (b) optimal switching duty cycle and pitch angle of the wind branch; and the resulting (c) power generations by the wind and solar branches; (d) angular velocity and normalized power coefficient of the wind turbine; and (e) batteries current.
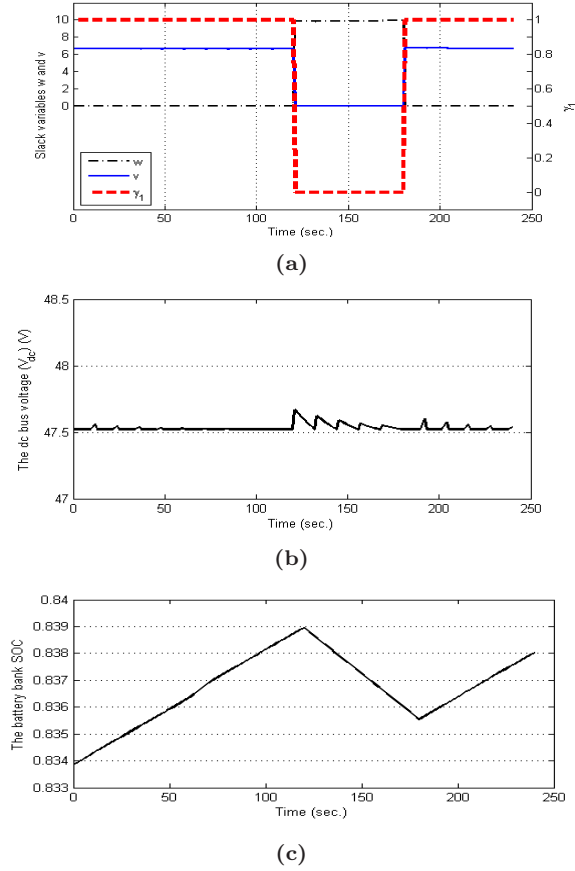
(a)

(b)

(c)

Fig. 8. (a) Switchings of the slack variables and the resulting (b) dc bus voltage level of the microgrid and (c) SOC trends.

(a)

(b)

Fig. 9. (a) Steady-state charging current of battery bank and the corresponding SOC and (b) dc bus voltage level of the microgrid.

rated power, excluding the time between 60 to 120 seconds, by the developed coordinated pitch and speed control strategy which operates as MPPT algorithm, unless there is excess generation. Since the maximum permissible charging currents of batteries are limited to $0.16C_{10}$, i.e. 7.2 A, the controller curtails the generated power of both the solar and wind branches between 60 to 120 seconds, when the load demand falls down, in order to charge batteries with a constant current of 7.2 A, as given in Fig. 7e.

Load demand steps up from 68% to 125% of its rated value at $t = 120$ seconds causing the battery bank switches from the charging to discharging operation mode. The consequent variations of the slack variables γ_1, v and w are given in Fig. 8a. Battery bank switches from the charging mode ($\gamma_1 = 1$) to the discharging mode ($\gamma_1 = 0$) in order to maintain the dc bus voltage level within the
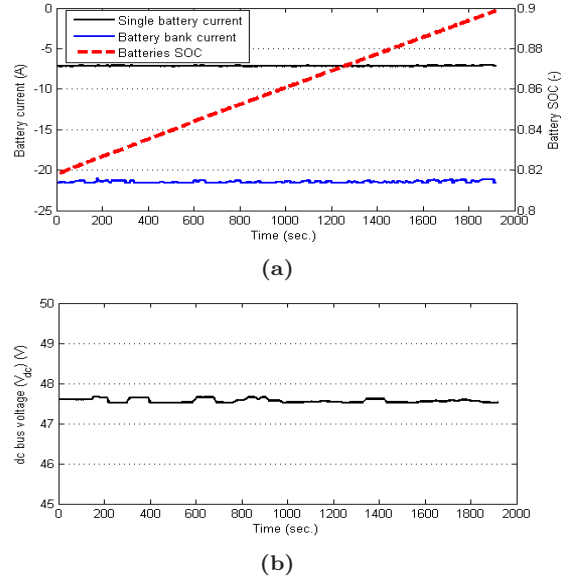
permissible range. Fig. 8b illustrates the fact that despite a substantial increase of the load demand, the dc bus voltage level remains in the range of $48.0 \pm 2\%$. Moreover, the variables v and w, which model the instantaneous direction changes of the battery current in Eq. (21), switch between 0 and the magnitude of the charging and discharging currents of batteries, respectively, which are limited to $0.16C_{10}$ and $0.23C_{10}$.

Fig. 8c illustrates that switching between the charging and discharging modes changes the SOC trends during the simulation time. The control strategy harvests the maximum available wind and solar powers in order to maximize SOC though SOC increases identically even when there is excess generation due to generation curtailment. Fig.s 9a and 9b show this fact with a long-term simulation results for the case in which wind speed and load demand remain steady at 1.08% and 67% of their rated values, respectively. Battery bank is charged with a constant current of $0.16C$ up to $SOC = 0.9$ and the dc bus voltage is maintained within its permissible range.

7. Conclusion

In this paper, standalone dc microgrids, consisting of the wind, solar, and battery branches, has

been mathematically modeled as complementarity dynamical systems. The proposed model has been used to develop a multivariable NMPC-based load tracking and voltage regulation strategy. Moreover, it has been declared as Modelica models and employed for long-term simulation of the standalone dc microgrid operations. The developed mathematical model is in the form of hybrid DAEs of the Filippov type, including mixed complementarity problems in order to model the multi-modal operation as well as the discontinuous cycle life state of the battery bank. The Modelica simulation results show the simulation accuracy with respect to the information available in manufacturers datasheets. The obtained results show that the developed Modelica model is accurate to simulate the hybrid nature of the standalone dc microgrids. Furthermore, the developed NMPC-based strategy for such a complementarity system is solved using general purpose NLP solvers. It is shown that such a strategy acts as a MPPT algorithm equipped with the generation curtailment facility to track the load demands and maintain the dc bus voltage level of the standalone dc microgrids.

8. Acknowledgment

References

[1] J. M. Guerrero, M. Chandorkar, T. Lee, and P. C. Loh. Advanced Control Architectures for Intelligent Microgrids–Part I: Decentralized and Hierarchical Control. *Industrial Electronics, IEEE Transactions on*, 60 (4):1254–1262, 2013. ISSN 0278-0046.

[2] P. Nema, R. K. Nema, and S. Rangnekar. A current and future state of art development of hybrid energy system using wind and PV-solar: A review. *Renewable and Sustainable Energy Reviews*, 13(8):2096 – 2103, 2009. ISSN 1364-0321.

[3] J. M. Guerrero, P. C. Loh, T. L. Lee, and M. Chandorkar. Advanced Control Architectures for Intelligent Microgrids–Part II: Power Quality, Energy Storage, and AC/DC Microgrids. *Industrial Electronics, IEEE Transactions on*, 60(4):1263–1270, 2013. ISSN 0278-0046.

[4] R. S. Balog, W. W. Weaver, and P. T. Krein. The Load as an Energy Asset in a Distributed DC SmartGrid Architecture. *Smart Grid, IEEE Transactions on*, 3(1): 253–260, 2012. ISSN 1949-3053.

[5] J. J. Justo, F. Mwasilu, J. Lee, and J. W. Jung. AC-microgrids versus DC-microgrids with distributed energy resources: A review. *Renewable and Sustainable Energy Reviews*, 24(0):387 – 405, 2013. ISSN 1364-0321.

[6] L. Grüne, and J. Pannek. *Nonlinear Model Predictive Control: Theory and Algorithms*. Communications and control engineering. Springer, 2011. ISBN 9780857295019.

[7] R. Findeisen, and F. Allgöwer. An Introduction to Nonlinear Model Predictive. In *Control, 21st Benelux Meeting on Systems and Control, Veidhoven*, pages 1–23, 2002.

[8] S. Schuler, D. Schlipf, P. W. Cheng, and F. Allgöwer. ℓ_1-Optimal Control of Large Wind Turbines. *Control Systems Technology, IEEE Transactions on*, 21(4): 1079–1089, 2013. ISSN 1063-6536.

[9] W. Qi, J. Liu, and P. D. Christofides. Distributed Supervisory Predictive Control of Distributed Wind and Solar Energy Systems. *Control Systems Technology, IEEE Transactions on*, 21(2):504–512, 2013. ISSN 1063-6536.

[10] L. Gkatzikis, I. Koutsopoulos, T. Salonidis. The Role of Aggregators in Smart Grid Demand Response Markets. *IEEE Journal on Selected Areas in Communications*, to apper, 2013.

[11] A. M. Dizqah, A. Maheri, K. Busawon, and A. Kamjoo. Modelling and Simulation of Standalone Solar Power Systems. *International Journal of Computational Methods and Experimental Measurements*, (in press) 2013.

[12] P. Fritzson. *Introduction to modelling and Simulation of Technical and Physical Systems with Modelica*. John Wiley & Sons, New York, 2011.

[13] P. Fritzson. *Principles of Object-Oriented Modeling and Simulation with Modelica 2.1*. Wiley, 2004. ISBN 9780471471639. URL http://books.google.co.uk/books?id=IzqY8Abz1rAC.

[14] A. F. Filippov, and F. M. Arscott. *Differential Equations with Discontinuous Righthand Sides: Control Systems*. Mathematics and its Applications. Kluwer Academic Publishers, 1988. ISBN 9789027726995.

[15] A. M. Dizqah, A. Maheri, K. Busawon, and P. Fritzson. Acausal Modelling and Dynamic Simulation of the Standalone Wind-Solar Plant Using Modelica. In *Computer Modelling and Simulation (UKSim), 2013 UKSim 15th International Conference on*, pages 580–585, 2013.

[16] L. T. Biegler. *Nonlinear Programming: Concepts, Algorithms, and Applications to Chemical Processes*. SIAM e-books. Society for Industrial and Applied Mathematics (SIAM, 3600 Market Street, Floor 6, Philadelphia, PA 19104), 2010. ISBN 9780898719383.

[17] W. P. M. H. Heemels, and B. Brogliato. The Complementarity Class of Hybrid Dynamical Systems. *European Journal of Control*, 9(2-3):322 – 360, 2003. ISSN 0947-3580.

[18] L. R. Petzold. A description of DASSL: a differential/algebraic system solver. In *Scientific computing (Montreal, Quebec, 1982)*, pages 65–68. IMACS, New Brunswick, NJ, 1983.

[19] P. Fritzson, P. Aronsson, H. Lundvall, K. Nyström, A. Pop, L. Saldamli, and D. Broman. The OpenModelica Modeling, Simulation, and Development Environment, 2005.

[20] H. Li, and Z. Chen. Overview of different wind generator systems and their comparisons. *Renewable Power Generation*, 2(2):123–138, 2008.

[21] H. Fakham, D. Lu, and B. Francois. Power Control Design of a Battery Charger in a Hybrid Active PV

Generator for Load-Following Applications. *Industrial Electronics, IEEE Transactions on*, 58(1):85 –94, jan. 2011. ISSN 0278-0046.

[22] O. Tremblay ,and L. Dessaint. Experimental Validation of a Battery Dynamic Model for EV Applications. *World Electric Vehicle Journal*, 3:10–15, 2009.

[23] N. Mohan, T. M. Undeland, and W. P. Robbins. *Power electronics: converters, applications, and design*. John Wiley & Sons, New York, 2 edition, 1995.

[24] M. Ashari and C.V. Nayar. An optimum dispatch strategy using set points for a photovoltaic (PV)-diesel-battery hybrid power system. *Solar Energy*, 66(1):1 – 9, 1999. ISSN 0038-092X.

[25] A. M. Dizqah, K. Busawon, and P. Fritzson. Acausal Modeling and Simulation of the Standalone Solar Power Systems as Hybrid DAEs. In *The 53rd Int'l Conf. of the Scandinavian Simulation Sociey (SIMS2012)*, 2012.

[26] J. J. Soon, and K. S. Low. Photovoltaic Model Identification Using Particle Swarm Optimization With Inverse Barrier Constraints. *IEEE Transactions on Power Electronics*, 27:3975–3983, 2012.

[27] M. G. Villalva, J. R. Gazoli, and E. R. Filho. Comprehensive Approach to Modeling and Simulation of Photovoltaic Arrays. *IEEE Transactions on Power Electronics*, 24:1198–1208, 2009.

[28] T. Burton, N. Jenkins, D. Sharpe, and E. Bossanyi. *Wind Energy Handbook*. John Wiley & Sons, West Sussex, UK, 2 edition, 2011.

[29] S. Heier. *Grid Integration of Wind Energy Conversion Systems*. John Wiley & Sons, 1998. ISBN 9780471971436.

[30] E. F. Camacho, and C. Bordons. *Model Predictive Control*. Advanced Textbooks in Control and Signal Processing. Springer-Verlag GmbH, 2004. ISBN 9781852336943.

[31] J. Andersson, J. Åkesson, and Moritz Diehl. CasADi – A Symbolic Package for Automatic Differentiation and Optimal Control. In Shaun Forth, Paul Hovland, Eric Phipps, Jean Utke, and Andrea Walther, editors, *Recent Advances in Algorithmic Differentiation*, volume 87 of *Lecture Notes in Computational Science and Engineering*, pages 297–307. Springer Berlin Heidelberg, 2012.

[32] J. M.Guerrero, J. C. Vasquez, J. Matas, L. G. de Vicuña, and M. Castilla. Hierarchical Control of Droop-Controlled AC and DC Microgrids–A General Approach Toward Standardization. *Industrial Electronics, IEEE Transactions on*, 58(1):158–172, 2011. ISSN 0278-0046.